ACS NANO

www.acsnano.org

ARTICLE

Electron Energy Loss Spectroscopy Investigation into Symmetry in Gold Trimer and Tetramer Plasmonic Nanoparticle Structures

Steven J. Barrow,[†,∥] Sean M. Collins,[‡,∥] David Rossouw,[§] Alison M. Funston,[⊥] Gianluigi A. Botton,[§] Paul A. Midgley,[‡] and Paul Mulvaney*[,†]

[†]School of Chemistry and Bio21 Institute, University of Melbourne, Parkville, Victoria 3010, Australia

[‡]Department of Materials Science and Metallurgy, University of Cambridge, 27 Charles Babbage Road, Cambridge CB3 0FS, United Kingdom

[§]Materials Science and Engineering, McMaster University, Hamilton, Ontario L8S 4L8, Canada

[⊥]Chemistry Department, Monash University, Clayton, Victoria 3800, Australia

Supporting Information

ABSTRACT: **We present a combined scanning transmission electron microscopy−electron energy loss spectroscopy (STEM−EELS) investigation into the mode symmetries of plasmonic nanoparticle trimer and tetramer structures. We obtain nanometer-resolved energy loss spectra for both trimer and tetramer structures and compare these to boundary element method simulations. We show that EELS, in conjunction with eigenmode simulations, offers a complete characterization of the individual superstructures, and we trace the evolution of both optically dark and bright modes and identify multipolar mode contributions. We then apply this technique to tetramer structures that exhibit an expanded range of mode symmetries for two-dimensional and three-dimensional self-assembled geometries. These findings provide a comprehensive experimental account of the available photonic states in self-assembled nanoparticle clusters.**

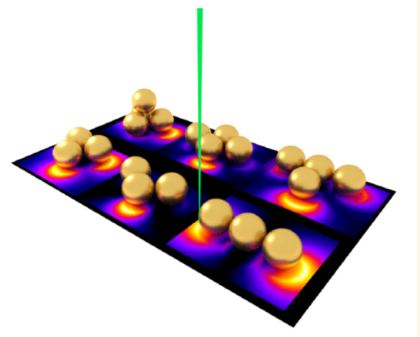

KEYWORDS: *STEM−EELS, surface plasmon, nanoparticle assemblies, non-negative matrix factorization, electron energy loss spectroscopy*

Planar arrangements of self-assembled nanoparticles have generated a substantial research following due to the unique surface plasmon phenomena they support. Circularly arranged nanostructures are of particular interest due to the accommodation of Fano-like resonances which can lead to enhanced localized electric fields in the vicinity of these structures.[1−3] Such field enhancements are useful in the amplification of Raman signals for chemical sensing,[4,5] and it has been proposed that circular two-dimensional (2D) nanoassemblies could be used for plasmon-based optical switching.[6] Moreover, three-dimensional (3D) nanostructures are predicted to be useful meta-materials with negative refractive indices that could have potential application in cloaking devices.[7−9] A comprehensive understanding of the surface plasmon modes in discrete plasmonic structures, the underlying states of these photonic systems, is essential for both understanding and optimizing the design of these nanoscale elements.

Plasmon coupling in small nanoparticle assemblies has been likened to that of molecular orbital theory, where plasmons from interacting particles can hybridize giving rise to "bonding" and "antibonding" states.[10] Discrete nanoparticle assemblies can thus be viewed as "plasmonic molecules", where the plasmon modes of individual nanoparticles behave collectively as a result of plasmon hybridization. Furthermore, the overall plasmonic behavior of discrete nanoparticle assemblies has been shown to be largely dependent on structure symmetry. Irreducible representations of nanoparticle assemblies, derived from group theory, have been demonstrated to provide a solid basis for understanding the plasmon modes of these systems.[11,12] However, the experimental observation of the plasmonic properties of such nanoparticle structures has been achieved predominantly with optical techniques.[7,11−16] Modes

Received: June 8, 2016
Accepted: August 2, 2016
Published: August 2, 2016

DOI: 10.1021/acsnano.6b03796
ACS Nano 2016, 10, 8552−8563

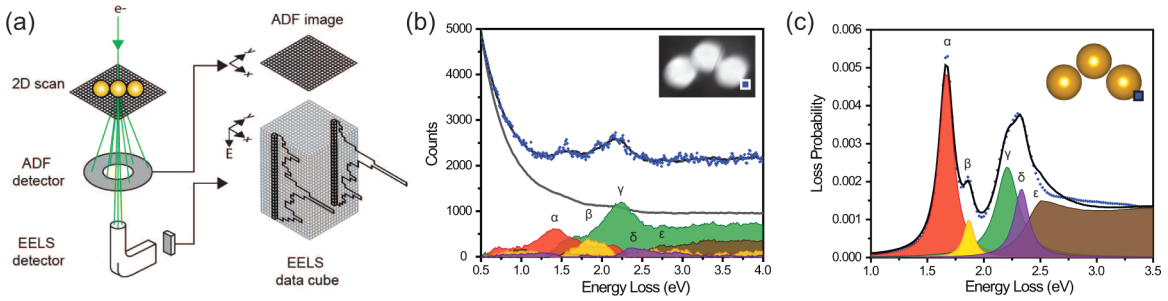

Figure 1. (a) Schematic of the EELS geometry. (b,c) Comparison between the experimental results (b) and BEM simulations (c) of a gold trimer consisting of 45 nm diameter spheres and a 55° semiangle is shown. The inset in (b) shows an ADF STEM image of the trimer. The blue dots represent the recorded signal, averaged over a 3 × 3 pixel area (shown as the blue squares in the insets). The black spectrum represents the sum of the model components. The gray component extracted by NMF in (b) represents the ZLP tail. For simulated EELS, the model consisted of four Lorentzian resonances (α–δ) and the gold loss function (ε).

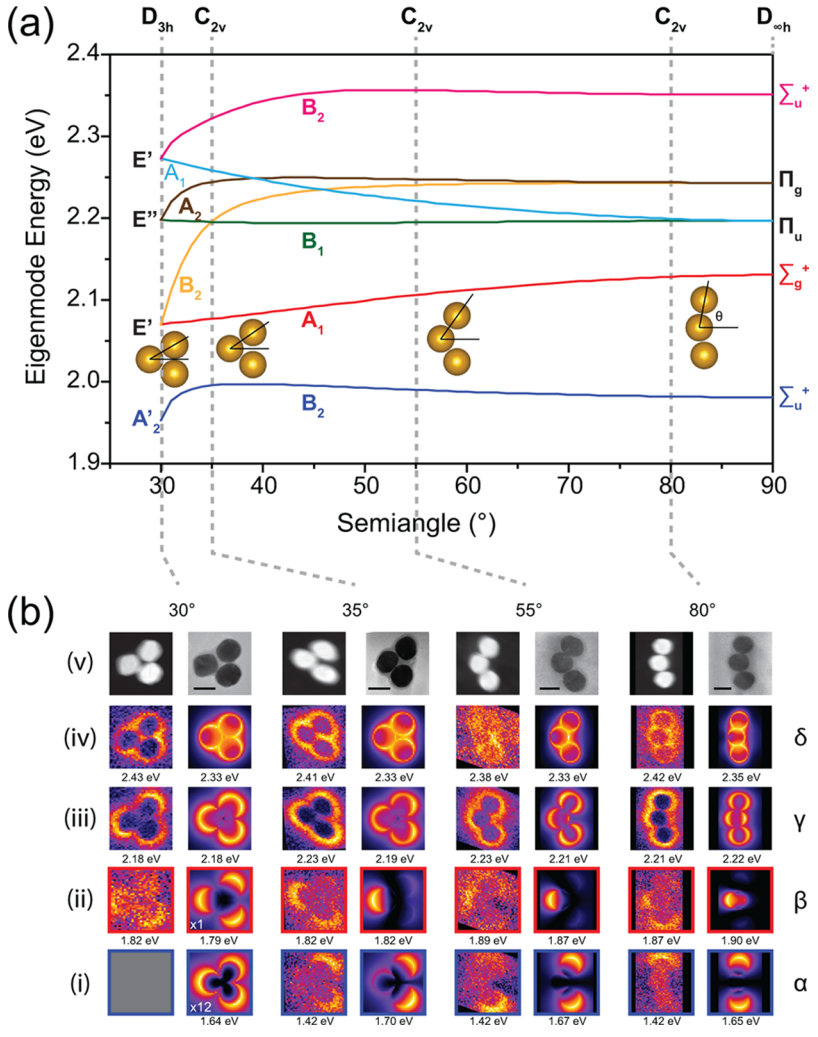

Figure 2. (a) Simulated eigenmode energies for systematic variation in the trimer semiangle as depicted in the overlaid schematic. Eigenmodes are defined in the quasi-static approximation. (b) (i–iv) Simulated (full BEM calculations with electrodynamic retardation effects) and experimental EELS maps of the plasmon modes detected in the nanosphere trimers, with corresponding ADF STEM and bright-field TEM images shown in (v). Scale bars are 50 nm. Gold nanospheres used in this work have diameters of approximately 45 nm. White numbers on the simulated EELS maps represent scaling factors. The simulated intensities for the 1.64 eV mode were low and are presented on a normalized intensity scale relative to the mode adjacent in energy (marked with a scaling factor of ×1). Greek letters correspond to NMF spectral factors corresponding to experimental maps (see also Figure 1 and Figure S2).

that do not interact with light due to their negligible dipole moment (termed "dark modes") cannot be easily probed optically. Optical effects that rely on coupling and interference between two or more modes (*e.g.*, Fano resonances) are consequently better understood by experimental measurements of both bright and dark plasmon modes.

DOI: 10.1021/acsnano.6b03796
ACS Nano 2016, 10, 8552–8563

Scanning transmission electron microscopy−electron energy loss spectroscopy (STEM−EELS) is an effective technique for the interrogation of dark modes.[17,18] The technique involves measuring the energy lost in a focused high-energy electron beam (80−300 keV) after interaction with a sample. When incident upon a metallic nanoparticle, a small amount of kinetic energy from the fast electrons can be transferred to the free electrons in the metal, leading to a collective plasmonic excitation of the electron gas and a characteristic energy loss in the transmitted beam.[19−21] This interaction of the electron beam with nanoparticle surface plasmons, combined with the subnanometer resolving power of the STEM technique, enables spatially resolved mapping of electron energy losses[22,23] and allows direct observation of plasmon modes that are inaccessible to optical techniques.[17] Furthermore, the STEM−EELS technique allows for the simultaneous morphological and spectral analysis of individual nanostructures, a significant advantage over current time-consuming methods used to correlate the optical scattering spectra with separate structural characterization by electron microscopy.[24−28] The spatial information obtained through EELS enables definitive mode assignments excited in assembled plasmonic structures. Single metal nanoparticles including spheres,[22,29,30] rods,[22,31] cubes,[32] bipyramids,[33] and nanowires[34−37] as well as nanoparticle dimers,[18,31,38] trigonal planar particle trimers,[39] and nanosphere chains[17] have been analyzed using STEM−EELS, but the technique has, to the best of our knowledge, yet to be applied for the systematic study of surface plasmon resonance modes in nonlinear 2D and 3D three-particle (trimer) and four-particle (tetramer) assemblies.

In this work, we present a comprehensive EELS investigation of the mode symmetries giving rise to surface plasmon excitations in trimers and tetramers. A complete analysis of the mode evolution of trimer structures upon ring-opening (*i.e.*, moving from a three-fold symmetric trimer to a linear chain trimer) informed by boundary element method (BEM) simulations and analyzed on the basis of point group irreducible representations is presented and compared to experimental EELS data. The addition of a fourth particle promotes a greater range of possible self-assembled geometries in the form of 2D and unique 3D structures. We investigate the role of tetramer symmetry for both in-plane (2D) and out-of-plane (3D) geometries, drawing on numerical simulations and experimental EELS spectrum imaging. In turn, we report modal symmetry assignments and the mode symmetry and energy evolution as a function of trimer and tetramer geometry. The results from the present study are discussed with reference to the optical response of similar structures throughout.[12] The combined systematic study of spatially resolved mode mapping and symmetry assignment by experimental EELS and eigenmode analysis enables correct assignment of mode contributions in these increasingly complex nanoparticle ensemble structures. These mode assignments are not possible directly from far-field spectroscopy or from simulations on a single structure, particularly due to the complex interplay and significant resonance energy shifts associated with geometric distortions. Our systematic mode symmetry analysis now outlines the optical design toolbox for three- and four-particle 2D and 3D nanophotonic structures.

RESULTS

EELS measurements on trimer and tetramer systems offer simultaneous spectral and spatial information about the plasmonic resonances of gold nanoparticle ensembles. Figure 1a displays a schematic of the experimental setup. The incident electron beam is scanned in a 2D raster over a region enclosing a nanoparticle cluster. At each point in the scan, the transmitted beam is collected by an annular dark-field (ADF) detector and an EELS spectrometer, resulting in the acquisition of an image and an EELS spectrum image data cube from the region. Figure 1b,c presents spectral analysis of EELS signals recorded from a trimer with a 55° semiangle between the terminal particles. This trimer has two mirror planes, one in the plane defined by the centers of each particle and a second mirror plane orthogonal to the first. The semiangle here is measured relative to the second orthogonal mirror plane, as additionally illustrated in Figure 2a. Figure 1b depicts electron energy loss from a selected area (3 × 3 pixels) recorded at the tip of the right terminal particle (blue square, inset). Non-negative matrix factorization (NMF) was applied to further decompose the entire spectrum image, and the separated spectral components are each presented according to their weighting at the selected trajectories.[40,41] Briefly, NMF decomposes the spatio-spectral data cube into a linear combination of spectral factors and corresponding amplitude maps, indicating the weighting of each spectral factor at each pixel. The black line shows the sum of all components. The corresponding amplitude maps are shown in Figure 2b. The NMF decomposition model reproduces the original data with high fidelity and significantly reduced noise. The background due to the spread in the incident beam energies, the zero loss peak (ZLP) tail, was recovered by NMF decomposition and separated from the energy losses due to excitation of surface plasmon resonances of the trimer. The spectra were further separated into four features attributed to the surface plasmon resonances (α−δ) and one further component (ε) attributed to the interband transitions of gold. These were identified according to the dominant peak or band edge signature in the spectral factor, and the center or edge onset was used to estimate the energy of the resonance (see also Figure 2b for experimental energies). While the numerical NMF algorithm returns spectral factors with some residual satellite peaks, most factors are dominated by a single peak or show the shape of the interband edge and bulk plasmon excitations expected for gold. Here, the symmetry, and accordingly the spatial distribution of the EELS intensity, and the relative peak energies are the key points of comparison for understanding the underlying mode structure. NMF is well-suited to this analysis despite imperfect peak shape recovery as it imposes minimal assumptions (non-negativity) on the data set and allows for separation of surface plasmon resonance features from an irregular background consisting of ZLP and bulk and interband transition contributions.

Each of the components α−ε was reproduced in BEM simulations of an ideal gold trimer consisting of 45 nm diameter gold spheres arranged with a 55° semiangle. The BEM simulations were performed using a purely real dielectric environment with no substrate (Figure 1c; see also Figure 2 and Figure S1). The simulated EELS signal was also modeled as the sum of four spectral features (α−δ) and the gold loss function (ε), fitted using four Lorentzian peaks with the loss function derived from the dielectric function reported by Johnson and Christy.[42] Minor discrepancies between the sum of the four Lorentzian components and the recorded signal in Figure 1c were observed at energies above 2.5 eV due to the truncation of the series of higher-order multipolar resonances

DOI: 10.1021/acsnano.6b03796
ACS Nano 2016, 10, 8552−8563

of metal spheres[43] not captured in the four lowest-energy peaks. The contribution of the gold bulk loss function is prominent in both the experimental and simulated cases. Furthermore, the relative energies of the four dominant contributions to the spectral features were reproduced in the simulation and in the experiment (see also Figure 2b). The relative intensity of the α component was lower in the experimental EELS than predicted by the simulated energy loss probability at a similar trajectory. However, substrate-, contamination-, and ligand-induced damping effects of low-energy resonances[44] and deviations from an ideal spherical geometry likely alter the relative intensities of each mode to a small degree. The experimental spectral components also appeared as broader peaks, consistent with higher damping as well as spectral broadening due to convolution with the ZLP.

Spectral factors for each NMF analysis are presented in Figure S2. Figure 2 presents a series of eigenmode calculations (defined exclusively in the quasi-static approximation) as well as a set of experimental and simulated EELS maps (full electrodynamical BEM calculations). The overlaid particle geometry schematics show four representative structures, tracking the evolution of three-fold symmetric trimer (left) to a linear chain trimer (right) *via* bent intermediate geometries. Each of these structures has been defined by the semiangle between the two terminal particles. These angles are shown on each of the schematics in Figure 2a, and the trimers were analyzed on the basis of point group irreducible representations. In this instance, a semiangle of 30° corresponds to the symmetric trimer of the D_{3h} point group; a 90° semiangle corresponds to a linear trimer of the $D_{\infty h}$ point group, and intermediate structures belong to the C_{2v} point group. The energy diagram plots the shifts in individual eigenmode energies as a result of the changing interparticle coupling for the geometry series. Surface charge diagrams for these mode evolutions are shown in the Supporting Information (Figure S1). Figure 2b(v) shows ADF STEM and bright-field TEM images of four gold nanoparticle trimers with semiangles of approximately 30, 35, 55, and 80° when moving from left to right, along with experimental and simulated EELS maps of these structures shown in Figure 2b(i–iv). Due to scan distortions during EELS acquisition, the ADF STEM and EELS maps were corrected by reference to the bright-field TEM images, giving rise to black regions where the images have been sheared, rotated, and cropped (see Methods). Critically, the EELS spectrum imaging results here allow for experimental mode assignment based on both spatial signal distributions as well as mode energies. Comparisons between simulations and experiments are common in far-field optical spectroscopy but do not allow for inspection of spatial signal distributions. In contrast, the direct comparisons between experimental EELS, BEM EELS simulations, and BEM eigenmode calculations presented here enable validation of mode symmetry assignments based on both spectral energies and spatial EELS signal distributions. These combined analyses are integral to the confident assignment of the observed surface plasmon modes identified by the experimental STEM–EELS mapping of trimers (Figure 2) and tetramers (Figure 4).

A detailed description of the trends shown in Figure 2a is given in the Supporting Information. Briefly, the trends in individual mode energies arise from the extent of interparticle coupling in the near-field; as the terminal particles separate with increasing semiangle, reduced coupling results in changes to mode hybridization and an increase in many of the trimer mode energies. In contrast, out-of-plane dipolar modes (*e.g.*, B_1 mode, Figure S1) exhibit minimal energy shifts as the in-plane semiangle does not alter hybridization of the individual particle modes significantly in this case. Figure 2b(i–iv) shows the EELS maps (both experimental and simulated) for the trimers shown in Figure 2b(v) that represent stages of this ring-opening process. These maps are plotted on a normalized scale to accommodate comparisons between experimental and simulated maps across a range of signal intensities. The normalization factors are presented in the Supporting Information (see Table S11). EELS intensities are not directly interpretable in terms of optical properties;[43] however, the underlying eigenmodes can be used to calculate optical responses to any incident electromagnetic field.[45]

The energies associated with the experimental EELS maps represent the energy of the dominant peak or band edge in the corresponding spectral factor (see Figure S2). The corresponding BEM simulations were performed in the fully retarded case rather than in the quasi-static approximation used for eigenmode simulations. An eigenmode decomposition of the retarded case has not been reported to date; however, the simulations accounting for retardation by considering the time-varying nature of the incident and induced fields provide the best possible model for comparison with experimental EELS. The resulting energies differ from the eigenmode energies due to retardation-induced red-shifting, but the underlying symmetries of the resonances are present in the simulations and in the experimental EELS maps. Beginning with the EELS maps shown in Figure 2b(i), the lowest-energy mode simulated for the D_{3h} trimer, with an energy of 1.64 eV, shows EELS intensity around the perimeter of the structure, with the EELS intensity reaching a maximum at the furthest point on each nanosphere from the center of the structure. The ring-like displacement current is characteristic of a magnetic mode,[1,46] and the symmetry of the mode was assigned to the A_2' irreducible representation in the D_{3h} point group. The A_2' mode was not detected experimentally *via* EELS due to poor coupling to the incident electron beam; hence an experimental EELS map for this mode is not shown. BEM simulations revealed the A_2' mode to exhibit substantially weaker interaction with the electron beam as the simulated A_2' mode map is scaled by a factor of 12 in Figure 2b(i) relative to the maximum EELS signal in the simulated map for the 1.79 eV mode in Figure 2b(ii). This magnetic mode was experimentally observed in an EELS study of 25 nm diameter silver particle trimers,[39] but the higher damping in gold due to its intrinsic dielectric properties,[42] the size-dependent variation in EELS intensity of surface plasmon excitations in spheres,[43] and the greater overlap with the ZLP tail for the 45 nm diameter gold particle trimers studied here preclude observation of this mode. However, by extending this investigation into a series of symmetry-broken trimers, the related B_2 mode derived from this magnetic mode of the perfectly symmetric trimer was observed in these self-assembled gold trimers.

As the semiangle of the trimer increases, and its symmetry alters to that of the C_{2v} point group, the A_2' mode transforms into a B_2 mode. This mode is evident for trimers with 35 and 55° semiangles, and the experimental and modeled EELS maps for these modes are shown in Figure 2b(i) with energies of 1.42 eV in the experimental data and 1.70 and 1.67 eV for the modeled maps. This discrepancy in energy (<0.3 eV) was attributed to incomplete modeling of the substrate and dielectric environment (see also Methods). The modeled

DOI: 10.1021/acsnano.6b03796
ACS Nano 2016, 10, 8552–8563

maps for these B_2 modes indicate that the EELS intensity decreases around the central nanoparticle, while the EELS intensity increases around the terminal nanoparticles. This trend is evident in the experimental EELS maps, although the EELS intensity is consistently weak near the central nanoparticle for all semiangles. The consistent observation of the B_2 mode across all gold trimer geometries extends previous analysis of this mode in silver nanoparticle aggregates.[46] Our EELS observations reveal that similar modes and mode hybridization effects occur in gold trimers. Although EELS generally does not record the asymmetric Fano line shape of such modes,[32,37] it does allow identification of the underlying resonance energies of hybrid modes, and our experimental evidence for the B_2 mode here establishes the feasibility of engineering Fano resonances using self-assembled gold trimers.

As the semiangle increases further, the B_2 mode of the C_{2v} trimer transforms into the Σ_u^+ mode of the linear trimer of the $D_{\infty h}$ point group. This mode is known as the longitudinal mode, or the super-radiant bright mode, and has been previously studied in linear nanoparticle structures *via* EELS.[17] The most linear trimer presented in this work exhibited a slight deviation from perfect linearity; thus the experimental EELS map for the mode at 1.42 eV in Figure 2b(i) (1.65 eV in the simulated map) is that of a B_2 mode. However, the EELS intensity of this mode closely resembles what would be expected for a Σ_u^+ mode, with an intense EELS signal observed around the ends of the trimer chain and minimal intensity recorded near the central nanoparticle. Although the experimental EELS map shows no signal around the end of the bottom-most nanoparticle, likely due to incomplete separation of the EELS intensities by NMF for the modes at 1.42 and 1.87 eV as well as imperfect modeling of the local ligand environment at each terminal nanoparticle,[17] the particle morphology, and substrate interactions. Still, the remarkably simple model of the sphere trimer in vacuum reproduces the energy and distinguishing spatial distribution features in the map of the quasi-linear experimental chain.

The simulated EELS map in Figure 2b(ii) for the E' modes at 1.79 eV for the D_{3h} trimer shows a similar intensity distribution to that of the A_2' mode; however, the EELS intensity is more localized at the tips of the nanoparticles. The experimental EELS map for this mode shows a very similar distribution of EELS intensity; however, the EELS signal around the top-most nanoparticle is less evident. Both the experimental and simulated energies for this mode agree (1.82 and 1.79 eV, respectively).

As the symmetry of the trimer is lowered to that of the C_{2v} point group, the lower-energy mode of the E' representation, a doubly degenerate set of dipolar modes in D_{3h} symmetry, converts to an A_1 mode, with the net dipole in the trimer aligned with the retained mirror plane in the C_{2v} geometry (see also Figure S1). The experimental and simulated EELS maps for this mode in the trimer with a semiangle of 35° can be seen in Figure 2b(ii), both with energies of 1.82 eV. Even the slight 5° change in the semiangle of the structure results in a drastic change for this mode, with the simulated EELS signal significantly reduced around the two-terminal particles in the trimer. The simulated EELS intensity is pronounced around the central nanoparticle, as expected for the symmetry-breaking of a pair of degenerate dipoles in the D_{3h} (E') to C_{2v} (A_1 + B_2) mode evolution. The experimental EELS map of the A_1 mode at 1.82 eV likewise shows a significant EELS signal around the central nanoparticle. Some EELS signal is recovered at the terminal particles, particularly the bottom-most particle in the experimental map. In the simulated map for the 1.82 eV mode (35°), the EELS intensity is significantly reduced at the terminal particles. The experimental relative intensities differ slightly; the ideal E' mode splitting is not reproduced perfectly in the approximately C_{2v} experimental trimer as fine-scale deviations from C_{2v} symmetry are not included in the simulation model. Similar observations can be made concerning the A_1 mode of the 55° semiangle trimer, with the experimental and simulated EELS maps presented in Figure 2b(iii), with energies of 1.89 and 1.87 eV, respectively.

When the semiangle of a trimer reaches 90°, the A_1 plasmon mode converts into a Σ_g^+ mode. This mode has also been described as the L2 subradiant mode, and for a perfectly linear trimer, the EELS map for this mode has been shown to exhibit signal around the central nanoparticle only.[17] Despite a 10° semiangle deviation from perfect linearity, the simulated EELS map shown in Figure 2b(ii) (1.90 eV) shows almost exclusive signal around the central nanoparticle as expected for the Σ_g^+ mode. The experimental EELS maps for this mode, which has an energy of 1.87 eV, also shows a signal localized near the bottom-most nanoparticle as well as near the central particle (see also discussion of 1.42 eV mode for the linear chain trimer).

As we begin to investigate the mode transformations in these trimers beyond the lowest-energy doubly degenerate E' representation, the mode assignment for the experimental EELS maps becomes difficult due to the intrinsic overlap of higher-energy modes. From 35° onward, A_1, A_2, B_1, B_2, and higher-energy modes occur at similar energies, giving rise to experimental EELS maps that contain contributions from more than one mode. While the two lowest-energy modes remain the lowest-energy modes for all considered geometries, eigenmode calculations (Figure 2a) show multiple energy crossings as a function of trimer geometry for the next five eigenmodes. In the trigonal planar trimer (D_{3h}), the higher-energy modes comprise an E'' and a further E' representation. In the linear chain trimer ($D_{\infty h}$), the modes comprise Π_u, Π_g, and Σ_u^+ symmetry representations. At intermediate geometries (C_{2v}), the E'' representation splits to B_1 and A_2 and the high-energy E' representation splits to A_1 and B_2. The B_1 (E'') and A_1 (high-energy E') modes decrease in energy and merge to become the Π_u representation in the linear chain. The A_2 (E'') mode joins the B_2 (low-energy E') mode to form the Π_g representation, and the B_2 (high-energy E') mode transforms to the high-energy Σ_u^+ representation. Due to this alternative mixing of doubly degenerate modes at the two extremes of the trimer geometry, there is particular overlap of modes for semiangles between 40 and 60° (B_1, A_1, B_2, and A_2 modes). As the geometry approaches one of the two extreme geometries, the modes separate into overlapping bands more similar to the perfectly degenerate eigenmode pairs. A series of higher-order multipolar modes appears at higher energies in addition to the seven lowest-energy modes considered here, but for relatively small spheres, these modes make minimal contribution to the EELS signal.[43]

Both the simulated and experimental EELS maps were decomposed into two spectral peak features in the energy window where the multiple high-energy modes dominate. The extent of each mode's contribution to the signal depends on the coupling efficiency to the electron beam, particularly the *z*-component of the electric field for the mode.[47] As a result, as the modes evolve, the relative intensities of each contribution

DOI: 10.1021/acsnano.6b03796
ACS Nano 2016, 10, 8552–8563

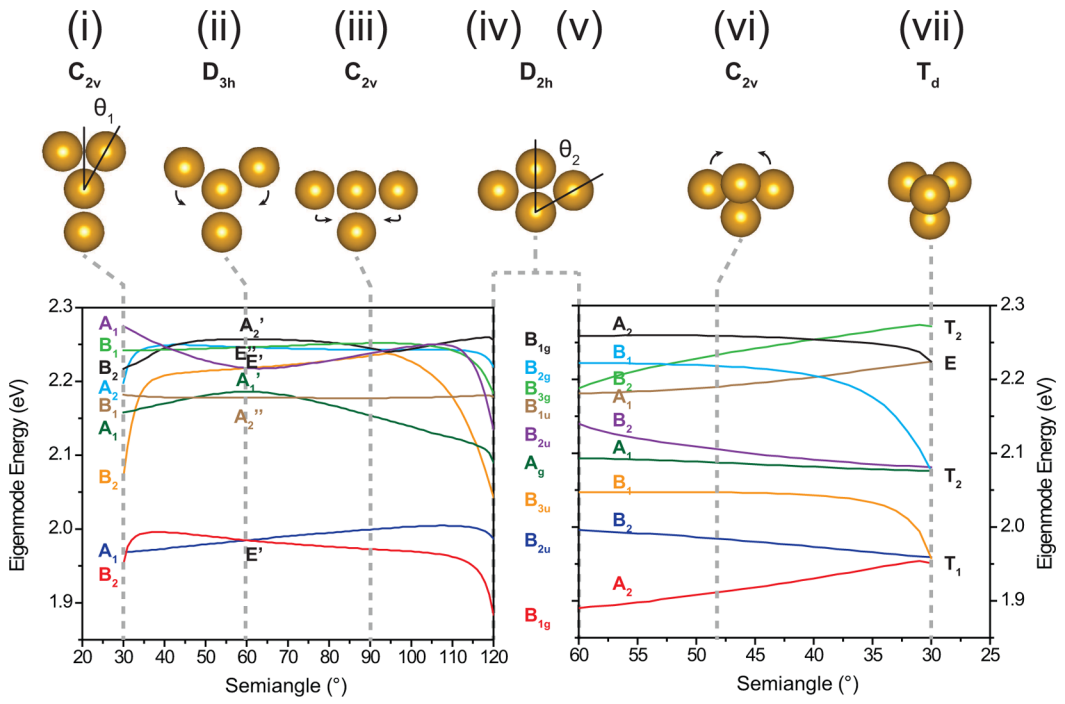

Figure 3. (Top) Series of schematics showing the symmetry evolution of a tetramer for in-plane (i–iv) and out-of-plane (v–vii) transformations. (Bottom) Corresponding plots of the energies of the plasmon modes of (left) tetramers (i–iv) and (right) tetramers (v–vii) for varying semiangles θ_1 and θ_2, respectively.

rise and fall, and so the contributions to each of the two separated spectral peaks change both as a function of the energy shifts due to the changes in mode symmetry and the coupling of the electron beam to the electric field resulting from the modal surface charge distribution. Moreover, due to these effects, the peak energies recorded for EELS maps do not follow a single trend in energy and do not track with the individual eigenmode energies. Generally, the low-energy signal and the high-energy signal observed were attributed to greater bonding and antibonding character, respectively, among this set of multiple overlapping multipolar modes.

The trimer mode analysis presented here as a function of the semiangle, in conjunction with the comparison of experimental EELS maps and full electrodynamic BEM simulations, enables the identification of the symmetry character associated with each map and its corresponding spectral signature by inspection of the underlying surface charge distributions associated with the modal EELS maps (see Figure S1). The net dipole moment, necessary for strong coupling in optical experiments, of each of the hybridized trimer modes varies as a function of semiangle. EELS mapping experimentally documents this evolution from bright dipolar modes to dark modes in key cases, such as the asymmetric, dipolar E'–A_1 mode's evolution to a dark, symmetric Σ_g^+ mode. Higher-order modes additionally include multipolar moments, exhibiting higher-frequency charge oscillations along the particle surfaces. These modes, while not strongly excited by light, are recorded in the experimental EELS data. The eigenmode decomposition in Figure 2a offers a complete modal representation in this case, further evidenced in the identification of each of the degenerate contributions to the doubly degenerate modes in the limiting cases of the trigonal planar D_{3h} (E-type modes) and linear $D_{\infty h}$ (Π-type modes) geometries. Since EELS measurements are sensitive to multipolar modes of spheres when optical measurements are not,[11,43] a complete eigenmode calculation is critical for the interpretation of EELS signals.

Tetramer geometries give rise to a substantially richer surface plasmon mode landscape due to the additional interparticle coupling introduced by the fourth particle as well as additional 3D conformational possibilities. The top of Figure 3 shows a series of tetramer structures, where the symmetry is altered both in-plane (i–iv) and out-of-plane (v–vii). Beginning with the in-plane series, structure (i) incorporates four nanoparticles in a "Y" configuration and is defined by a semiangle of $\theta_1 = 30°$, as seen in the schematic in Figure 3. This structure belongs to the C_{2v} point group. The point group then changes to D_{3h} as the semiangle increases to 60° (structure (ii)) and then to C_{2v} with a semiangle of 90° (structure (iii)), where the tetramer resembles a "T" shape, before assuming D_{2h} symmetry with a semiangle of 120° (structure (iv)).

Structures (v–vii) represent a further symmetry transformation series for out-of-plane geometries. Beginning with the D_{2h} tetramer (structure (v)), we redefine the semiangle as $\theta_2 = 60°$, the supplementary angle to the semiangle defined for structure (iv). The supplementary semiangle becomes the convenient angular reference for out-of-plane movement of the top-most particle (structure (v)). In modeling the evolution of structures (v–vii), the top-most particle is lifted on top of the structure, while the left-most and right-most particles are then tucked under the top-most particle with a fixed interparticle spacing to give a tetramer of the C_{2v} point group with a semiangle of 45° (structure (vi)). These particles then continue their respective movements, such that a fully symmetric tetrahedral structure (T_d point group) is obtained with a semiangle of 30°. These particle movements were selected to gradually transform the particle ensemble geometry between the experimentally observed tetramer structures shown in Figure 4a. Such a gradual perturbation allows for the systematic tracking of the eigenmodes, where small changes in mode

DOI: 10.1021/acsnano.6b03796
ACS Nano 2016, 10, 8552–8563

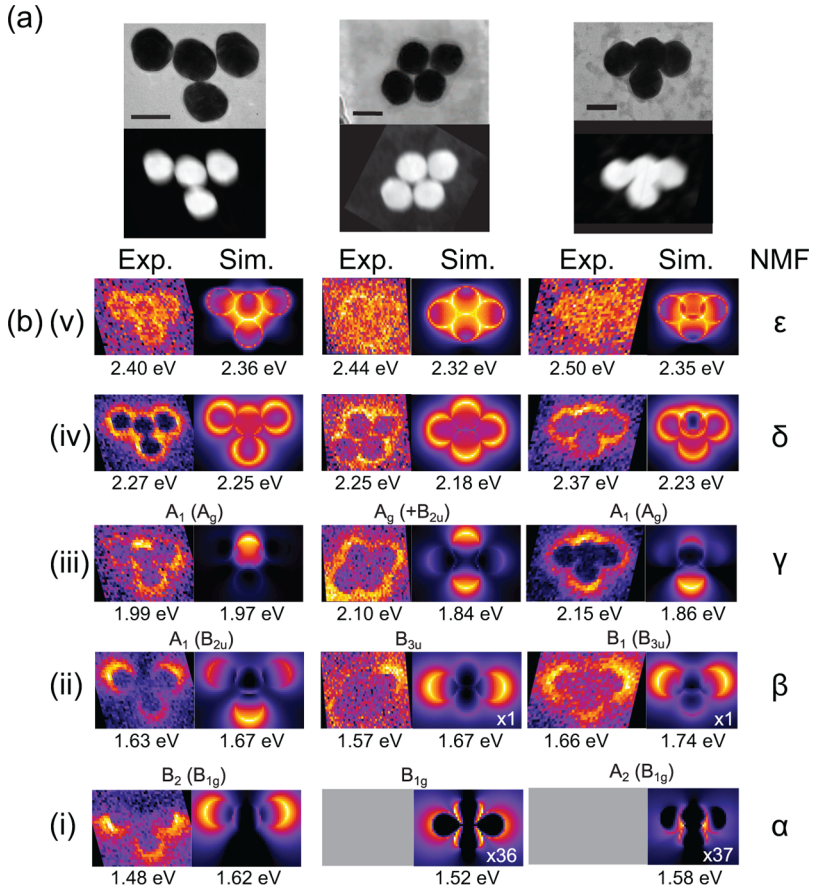

Figure 4. (a) Bright-field TEM and dark-field STEM images of the tetramers are shown: a 2D C_{2v} tetramer (left), a D_{2h} tetramer (middle), and a 3D C_{2v} tetramer (right). Scale bars are 50 nm. (b) Experimental and BEM simulated (retarded calculations) EELS maps for the tetramers in (a) are shown. The colored boxes surrounding the EELS maps coordinate with the plots depicted in Figure 3. Gold nanospheres used in this work have diameters of approximately 45 nm. White numbers on the simulated EELS maps represent scaling factors. The simulated intensities for these modes were low and are presented on a normalized intensity scale relative to the mode adjacent in energy (marked with a scaling factor of ×1). Greek letters correspond to NMF spectral factors corresponding to experimental maps (see also Figures S8 and S9).

energy and surface charge distribution facilitate comparison between independent simulations and classification of each mode with a transforming irreducible representation.

Figure 3 also shows two simulated energy diagrams that highlight the dependence of mode energy in tetramer structures on the semiangle for both the in-plane (left) and out-of-plane (right) transformations. The nine lowest-energy modes are shown in each case, and surface charge diagrams of the mode evolutions are shown in the Supporting Information (in-plane, Figure S3; out-of-plane, Figure S4) along with a description of the mode evolutions for each case.

Figure 4a shows bright-field TEM and ADF STEM images of three tetramer structures. As for the trimer maps, scan distortions during the EELS acquisition were removed by reference to the bright-field TEM images of the same structures (see also Methods). The left-most structure represents a 2D tetramer of the C_{2v} point group, comparable to structure (iii) in Figure 3. There is some deviation from the ideal left−right mirror-plane symmetry in the experimental structure (left) relative to structure (iii) in Figure 3. However, this distortion only perturbs the underlying mode states slightly and gives rise to modes with similar energies and spatial distributions (see Figure S7). For the purpose of comparison with the D_{3h}−C_{2v} transformations common to both the trimer and tetramer systems, the mirror-symmetric structure (iii) is shown to reasonably represent the modes in the experimental structure (left). The middle tetramer is representative of a D_{2h} tetramer, which is shown in Figure 3 as structures (iv) and (v). The final tetramer on the right in Figure 4a is another C_{2v} tetramer but now similar to structure (vi) in Figure 3 with one particle out-of-plane. Such a tetramer is necessarily described as 3D, offering a further tuning parameter to its near- and far-field optical response.

Experimental and simulated EELS maps for these tetramers are highlighted in Figure 4b. The energies given for the experimental maps refer to the energy at the dominant peak maximum or band edge identified in NMF spectral factors (see Figures S8 and S9). In spite of the experimental challenges for these data sets, including background contributions from the ZLP, interband transitions and bulk plasmon excitations in gold, and experimental noise, experimental maps were generally in good agreement with simulations. Some of the spatial intensity distributions deviated from simulated maps, particularly in the relative intensities (*e.g.*, (ii) on the left, the 2D C_{2v} tetramer) or additional intensity in the experimental map (*e.g.*, (iii) in the middle, the 2D D_{2h} tetramer), attributed to incomplete separation of modes adjacent in energy and to deviations from the idealized spheres used to model particle geometries. The experimental maps, however, consistently show a combination of similar peak energies and similar

DOI: 10.1021/acsnano.6b03796
ACS Nano 2016, 10, 8552−8563

symmetries in the distribution of spatial intensity for the dominant spectral features anticipated from simulations. These considerations enable the identification of the dominant underlying mode states (irreducible representations) of interest.

Figure 4b(i) shows EELS maps of the lowest-energy modes. The 2D C_{2v} tetramer has a mode with an energy of 1.48 eV, and the simulated EELS map for this mode is shown next to it, with an energy of 1.62 eV. The simulated EELS map exhibits the highest EELS signal around the left-most and right-most nanoparticles aligned horizontally with the three-particle backbone of the structure. This is reflected in the experimental EELS map for this mode, with intensity highest at opposite ends of the three-particle backbone. However, the EELS signal is only evident around the lower half of these particles, and some EELS signal is evident around the bottom-most particle in the structure, partially explained by the deviation in left−right mirror symmetry in the experimental geometry (see Figure S7). Experimentally, the two lowest-energy modes, with an energy separation of approximately 0.1 eV, were not fully resolvable as the energy separation was on the same order as the energy resolution of the microscope. This narrow energy separation is consistent with the simulated peak energies. As a result, the experimental EELS maps exhibit some similarity in spatial intensity features. The NMF decomposition identifies subtle differences in the spatial distribution of intensity, particularly at the left- and right-most particles, and in the recorded spectra to reveal the presence of two separate modes.

The lowest-energy modes for the D_{2h} and 3D C_{2v} tetramers were not observed experimentally; however, the simulated EELS maps for these modes are shown in Figure 4b(i) (middle and right modes, respectively). These simulated maps exhibit maximum EELS intensities of less than 3% of the magnitude of the maximum EELS signals simulated for higher-energy modes in Figure 4b(ii) (B_{3u} and B_1 modes). They represent a negligible fraction of the energy loss probability for experimental EELS. The second lowest-energy modes expected for these structures (A_1−B_{2u}−B_2, dark blue line in Figure 3) were not observed in simulation or experiment due to their minimal contribution to the EELS signal. For the D_{2h} tetramer, the lowest-energy B_{1g} mode has an energy of 1.52 eV and shows an EELS signal around the left-most and right-most nanoparticles, with the EELS signal also partially present around the top and bottom nanoparticles in this structure. The simulated EELS map for A_2 (B_{1g}) mode of the 3D C_{2v} tetramer is also shown in Figure 4b(i), with an energy of 1.58 eV. The map shows EELS intensity near the central cavity of the tetramer structure.

Figure 4b(ii) displays the next series of experimental and simulated EELS maps obtained for the tetramer structures. The experimental EELS map for the 2D C_{2v} tetramer has an energy of 1.63 eV, which closely matches the energy of the simulated EELS map (1.67 eV). This mode is the A_1 (B_{2u}) mode and exhibits an EELS signal at the tips of each of the three outermost nanoparticles (pointing away from the center of the structure rather than aligned with the three-particle backbone as in (i)). While this is also true of the simulated EELS map, the strongest EELS signal is present at the bottom-most particle in the simulated map, whereas the bottom-most particle in the experimental map shows the weakest EELS signal. This discrepancy was attributed to incomplete separation of the A_1 and B_2 modes in the 2D C_{2v} geometry as they were separated by approximately 0.1 eV experimentally.

The experimental and simulated EELS maps for the D_{2h} tetramer in Figure 4b(ii) were assigned to the B_{3u} irreducible representation, with energies of 1.57 and 1.67 eV, respectively. The simulated EELS map for this mode shows an EELS signal around the left-most and right-most nanoparticles only, a spatial distribution also recorded in the experimental EELS map though the signal is weak around the left-most nanoparticle. Without consideration of the underlying mode evolution due to the tetramer symmetry, the appearance of such a seemingly "longitudinal" mode in the D_{2h} geometry is spatially similar to the lowest-energy mode (B_2) for the C_{2v} geometry. However, the symmetry analysis presented here demonstrates that the "longitudinal" dipole modes for each tetramer have distinct modal origins and do not belong to a single evolving mode. In this case, careful symmetry analysis is necessary for complete accounting and correct assignment of the tetramer modes.

The EELS maps for the 3D C_{2v} tetramer in Figure 4b(ii) represent the B_1 mode, which stems from the B_{3u} mode of the D_{2h} tetramer. With energies of 1.66 and 1.74 eV, respectively, the experimental and simulated EELS maps for this mode agree, with an EELS signal present around the left-most and right-most nanoparticles and a weaker signal present around the bottom nanoparticle.

At higher energy (Figure 4b(iii)), the EELS maps for the 2D C_{2v} tetramer correspond to the A_1 (A_g) mode. Both the energies and EELS signals match the experimental and simulated EELS maps of this mode, with energies of 1.99 and 1.97 eV for the experimental and simulated maps, and the strongest EELS signal is present around the central nanoparticle in the three-particle backbone of the tetramer. The experimental and simulated EELS maps for the D_{2h} tetramer with energies of 2.10 and 1.84 eV, respectively, in Figure 4b(iii) were assigned to the A_g mode. The simulated EELS map for this mode shows an EELS signal around the top- and bottom-most nanoparticles in the tetramer, whereas the experimental EELS map exhibits a signal around the entire structure. Based on a comparison with single-mode maps, the simulated map likely contains contributions from the higher-energy B_{2u} mode (purple line, Figure 3), adding an emphasis to the strong signal at the top and bottom particle. The experimental map likely shows a more even intensity around all particles due to incomplete separation from other modes adjacent in energy, a more prominent contribution from the A_g mode, or other deviations from the perfect four-sphere model. The final mode in Figure 4b(iii) is the A_1 mode of the 3D C_{2v} tetramer, which evolves from the A_g mode of D_{2h} tetramer. The experimental and simulated EELS maps for this mode have energies of 2.15 and 1.86 eV, and the EELS signal present in both agrees, with a strong signal at the top and bottom nanoparticles in each map. The experimental observation of this family of A_g modes is a particularly significant observation by EELS as it represents a totally symmetric "dark" mode that exhibits a negligible dipole moment for many geometries.

The EELS maps evident in Figure 4b(iv) for the 2D C_{2v} tetramer match in both energy (2.27 and 2.25 eV, respectively) and the spatial distribution of the EELS signal. Both of these maps show an EELS signal around the entire perimeter of the structure. The modes of the D_{2h} and 3D C_{2v} tetramers in Figure 4b(iv) exhibit similar spatial distributions of the EELS signal. The energies for the experimental and simulated maps for these structures match, and the EELS signal is again present around each of these structures. Notably, the EELS signal is present around the entire circumference of the top nanoparticle of the

DOI: 10.1021/acsnano.6b03796
ACS Nano 2016, 10, 8552−8563

3D tetramer in the simulated EELS map, but the EELS signal does not completely encircle the top particle in the experimental map. This minor discrepancy can be attributed to additional attenuation of the electron beam for trajectories penetrating the nanoparticles and correspondingly weaker EELS signals recorded for these trajectories.

Figure 4b(v) contains the final series of modes detected experimentally in the tetramers presented. Each of these modes presents a similar EELS spatial pattern and shall therefore be discussed simultaneously. The simulated EELS maps for these modes (with energies of 2.36, 2.32, and 2.35 eV for the 2D C_{2v}, D_{2h}, and 3D C_{2v} tetramers, respectively) all show an EELS signal concentrated at the gaps between the spheres in the structure. Although the EELS signal evident in the experimental EELS map for the 2D C_{2v} tetramer (2.40 eV) matches that for the simulated EELS map, the experimental maps for the D_{2h} tetramer and the 3D C_{2v} tetramer are generally too noisy for direct comparison. Experimentally, these spectral features are not distinguished from the interband transition edge of gold (see also Figure 1) and therefore contain contributions from bulk and from surface plasmon modes at energies overlapping the interband edge onset. The corresponding spatial distribution of the surface plasmon modes, separated in simulations, is only weakly imprinted on the experimental maps as the surface plasmon signals are only a minor contribution to the total EELS signal at these energies.

The presented analysis of experimentally observed self-assembled tetramers in 2D and 3D configurations in the context of eigenmode calculations and group theoretical symmetry classification identified the principal, lowest-energy dark and bright modes in gold nanosphere tetramers and clarified the distinct modal origins of the prominent resonances observed for different arrangements of the subunits within the ensemble. The out-of-plane transformations also serve to corroborate and extend far-field scattering studies of similar 3D tetramer assemblies exhibiting Fano resonances involving the dipole resonances of the cluster.[7] Whereas optical far-field scattering reveals Fano line shapes in such structures,[7] EELS can actually isolate and identify the contributing modal resonances that ultimately interact in the far-field.[37] Validated by comparison with experimental EELS of 3D tetramer structures, our simulations of these structures go beyond simple mode assignments and enable decomposition and analysis of the contributing eigenmodes.

CONCLUSIONS

In summary, we have examined surface plasmon symmetries, energies, and mode splitting and crossing behavior in trimer and tetramer nanoparticle structures using STEM−EELS mapping and eigenmode analysis. First, mode symmetries have been assigned to trimer structures by comparing experimental EELS maps and BEM simulations; furthermore, both mode splitting and energy shifts have been documented. We have shown that EELS, in conjunction with NMF spectral processing and BEM simulations, offers comprehensive plasmon mode analysis, including experimental tracking of both optically dark and multipolar modes. Mode assignments have been reported for self-assembled tetramer structures, including consideration of both the in-plane and out-of-plane alterations to the particle aggregate symmetry. Changes in the major mode contributions to the lowest-energy modes for 2D and 3D configurations have been explained by symmetry analysis. This systematic assignment of mode symmetries for experimental gold trimers and tetramers presents a demonstration of the consistent set of symmetry states, tracked as irreducible representations, underpinning multiparticle surface plasmon resonances for real permutations encountered in nanoparticle self-assembly. The present work highlights the experimentally available photonic states in three- and four-particle aggregates. Together, these experimentally documented photonic states form a library or a toolbox for optical engineering, enabling further optical designs incorporating Fano or magnetic resonances with gold nanoparticle superstructures.

METHODS

Chemicals and Gold Nanosphere Preparation. Gold(III) chloride trihydrate (99.9+%) and tris(2-carboxyethyl)phosphine hydrochloride (TCEP) were purchased from Sigma-Aldrich. All oligonucleotides were purchased from Geneworks. Cetyltrimethylammonium bromide (CTAB) was purchased from Ajax Chemicals. Spherical gold nanoparticles were prepared using the wet chemical synthesis developed by Rodríguez-Fernández *et al.*[48] Briefly, citrate seeds were prepared by bringing 100 mL of aqueous 0.25 mM chloroauric acid ($HAuCl_4$) to boiling temperature. Seed growth is initiated by the addition of 3.5 mL of aqueous 1 wt % sodium citrate solution. A deep red color after 5 min of boiling indicated the presence of gold nanoparticle seeds. Growth solutions were then prepared by adding 1 mL of approximately 1 mM range concentration of aqueous $HAuCl_4$ to 88 mL of 0.015 M CTAB. One milliliter of ascorbic acid was then added. The concentration of ascorbic acid was adjusted so that a 2:1 ratio of ascorbic acid to $HAuCl_4$ was present. Ten milliliters of seed solution was then added to initiate growth of the seeds followed by stirring for a few minutes. The concentration of $HAuCl_4$ needed was calculated from the volume of gold required to grow the 17 nm diameter seeds to the desired diameter.

Self-Assembly. The nanoparticles were assembled using thiolated single-strand oligonucleotides *via* a method adapted from the work of Yao *et al.*[49] Thiolated oligonucleotide strands (purchased from Geneworks) were reduced with TCEP and added to nanoparticle solutions to achieve a maximum DNA coverage. To form the oligonucleotide-functionalized nanoparticles, 5 μL of an oligonucleotide solution (100 μM in oligomer concentration) was added to 45 μL of a 200 μM TCEP solution. The resulting solution was left for 30 min to allow reduction of the terminal thiol moiety on the oligonucleotide. The reduced oligonucleotide solution was then added to 1000 μL of a solution of gold nanoparticles (generally 30−60 nm in diameter) and concentrations of approximately 6×10^{10} particles/mL. Equal volumes of nanoparticles functionalized with separate complementary DNA strands (e.g., S1-functionalized nanoparticles and S2-functionalized nanoparticles for the assembly of dimers and chains) were then mixed together. Generally, volumes of each sample between 250 and 500 μL were used. Assembly reactions were then initiated by adding 3 mL of 0.1 M phosphate-buffered saline to the mixed nanoparticles. After the assembly reaction had proceeded for 1 min, the assembled particles were drop-coated onto plasma-cleaned carbon TEM grids. Once the sample had been allowed to sit for a minute, the TEM grid was dried under a stream of N_2 and was then placed in a water bath at room temperature for 5 min, then removed and dried with a steady stream of N_2.

EELS Characterization. EELS signals were acquired from gold nanoparticles and nanoparticle chains using an FEI Titan 80-300 TEM equipped with a monochromator and a high-resolution spectrometer and operated at 80 keV. Particle imaging was performed in both parallel beam and scanning beam modes. In parallel beam mode, bright-field micrographs were acquired. Analysis of the particle optical properties, however, was performed in scanning beam mode, where the electron beam is focused to a point (approximately 2 nm in diameter) and scanned to form an image. In this mode, local EELS spectra can be recorded from a small excited volume by collecting low-angle scattered electrons and a dark-field image can be formed

DOI: 10.1021/acsnano.6b03796
ACS Nano 2016, 10, 8552−8563

(simultaneously) by collecting high-angle scattered electrons with an annular detector. By raster scanning the beam, both structural and spectral information can be gathered from a region of interest in an approach termed spectrum imaging, forming a powerful means for rapid materials characterization at the nanometer level.[50] Distortions in the electron beam scan during STEM spectrum image acquisition were apparent by comparison of STEM images and TEM bright-field micrographs acquired separately. Scan distortions were removed by registering the image pixels in the STEM micrographs to the corresponding structures in bright-field TEM images, aligned using affine image transformation routines in Matlab. The micrographs were then cropped and rerotated for optimal comparison with simulated maps.

Spectral Processing. Spectral processing was performed using Hyperspy,[45] an open-source software coded in Python. Spikes due to X-rays striking the charge-coupled device detector were removed using a routine that automatically identified outlying high-intensity pixels and performed interpolation in the spectral region after removal of the spike. Spectra were then aligned to subpixel accuracy using a correlation routine on the ZLP and cropped to the energy window of interest (0.5 to 4.0 eV). NMF decomposition was performed as reported previously.[32,33,37] The number of components retained in the decomposition was chosen following repeated decompositions using a range of components. The number of components was selected in order to eliminate only those components containing high spatial frequency noise. Principal-component analysis scree plots showed that a similar number of components was needed to describe the data sets.

Modeling. BEM simulations were carried out using the Matlab-based MNPBEM toolbox,[51] which solves Maxwell's equations for arbitrary geometries using surface charges and currents. For simulations of the energy loss probability, spheres were modeled with a triangular mesh consisting of 508 faces and simulations were performed to solve the full Maxwell's equations (including retardation effects). The spheres were defined with a diameter of 45 nm and an intersphere spacing of 1 nm. For quasi-static eigenmode calculations, the mesh density was increased to 1054 faces for each sphere and the intersphere spacing was set to 3 nm to minimize the introduction of artifacts due to the mesh in the eigenvalue solver. The trimer and tetramer geometries were further defined by fixing the intersphere spacings and translating the sphere centers to the geometry defined by the appropriate semiangle. In order to extract integrated peak maps comparable to NMF experimental EELS maps, peak fitting was performed on the simulated spectrum images in Hyperspy. Lorentzian peaks were used to model each of the noted surface plasmon peaks, and the loss function $\Gamma^{\mathrm{EELS}} \propto \mathrm{Im}\left\{\frac{-1}{\epsilon(\omega)}\right\}$ calculated from the dielectric function $\epsilon(\omega)$ given in ref 42 was used to model the bulk losses. In order to account for red-shifting effects due to the dielectric environment of the carbon support film, a purely real dielectric constant of 2.56 (refractive index $n = 1.6$) was assigned to the ambient medium in the BEM simulations. The dielectric environment of a support film and the surrounding surfactant layer primarily act to lower the energy of surface plasmons in noble metal nanoparticles,[17,37] and the selected dielectric constant was found to reasonably match experimental energies across the trimer and tetramer structures examined.

Single-mode calculations are possible for eigenmode calculations because the total energy loss probability can be expressed as a sum over individual modes i:[47]

$$\Gamma^{\mathrm{EELS}}(\mathbf{R}_0, \omega) = \sum_i C_i(\omega) \left| \oint \mathrm{d}\mathbf{s} \phi^*_{\mathbf{R}_0}(\mathbf{s}) \sigma_i(\mathbf{s}) \right|^2 \quad (1)$$

where the integral is over the surface differential $d\mathbf{s}$, $\phi_{\mathbf{R}_0}(\mathbf{s})$ is the potential of the exciting electron traveling along a trajectory defined in the plane perpendicular to the trajectory by the coordinate $\mathbf{R}_0$, $\sigma_i(\mathbf{s})$ is the surface charge along the surface $\mathbf{s}$, and $C_i(\omega)$ is a frequency-dependent coefficient for eigenmode i. Single-mode maps were generated using an implementation of eq 1 in Matlab, where the sum is taken over a single-mode i only.

ASSOCIATED CONTENT

Supporting Information

The Supporting Information is available free of charge on the ACS Publications website at DOI: 10.1021/acsnano.6b03796.

Detailed descriptions of the mode evolutions of trimer and tetramer nanostructures, calculated surface charge evolutions of trimer and tetramer nanostructures, NMF spectral factors, demonstration of using single-mode maps in the assignment of plasmonic modes, the effect of deviations from an ideal C_{2v} tetramer geometry, and maximum EELS probabilities for trimer and tetramer simulated maps (PDF)

AUTHOR INFORMATION

Corresponding Author

*E-mail: mulvaney@unimelb.edu.au.

Author Contributions

‖S.J.B. and S.M.C. contributed equally to this work.

Notes

The authors declare no competing financial interest.

ACKNOWLEDGMENTS

S.J.B. thanks the University of Melbourne for a MATS scholarship and the Ernst and Grace Matthaei research scholarship. S.M.C. acknowledges the support of a Gates Cambridge Scholarship. D.R. acknowledges support from the Royal Society's Newton International Fellowship scheme. P.A.M. acknowledges support from the European Research Council under the European Union's Seventh Framework Program (No. FP7/2007-2013)/ERC Grant Agreement No. 291522-3DIMAGE and the European Union's Seventh Framework Program under a contract for an Integrated Infrastructure Initiative (Reference No. 312483-ESTEEM2). P.M. acknowledges Australian Research Council (ARC) support through LF 100100117. A.M.F. would like to thank the ARC for support *via* FT110100545 and DP120101573. G.A.B. is grateful to the Natural Sciences and Engineering Research Council (NSERC), Canada, for a Discovery grant supporting this work. The electron microscopy was carried at the Canadian Centre for Electron Microscopy, a national facility supported by the Canada Foundation for Innovation under the MSI program, NSERC and McMaster University.

REFERENCES

(1) Fan, J. a.; Wu, C.; Bao, K.; Bao, J.; Bardhan, R.; Halas, N. J.; Manoharan, V. N.; Nordlander, P.; Shvets, G.; Capasso, F. Self-Assembled Plasmonic Nanoparticle Clusters. *Science* **2010**, *328*, 1135−1138.

(2) Fan, J. a.; Bao, K.; Wu, C.; Bao, J.; Bardhan, R.; Halas, N. J.; Manoharan, V. N.; Shvets, G.; Nordlander, P.; Capasso, F. Fano-Like Interference in Self-Assembled Plasmonic Quadrumer Clusters. *Nano Lett.* **2010**, *10*, 4680−4685.

(3) Fan, J. a.; He, Y.; Bao, K.; Wu, C.; Bao, J.; Schade, N. B.; Manoharan, V. N.; Shvets, G.; Nordlander, P.; Liu, D. R.; Capasso, F. DNA-Enabled Self-Assembly of Plasmonic Nanoclusters. *Nano Lett.* **2011**, *11*, 4859−4864.

(4) Lim, D.-K.; Jeon, K.-S.; Kim, H. M.; Nam, J.-M.; Suh, Y. D. Nanogap-Engineerable Raman-Active Nanodumbbells for Single-Molecule Detection. *Nat. Mater.* **2010**, *9*, 60−67.

(5) Eggeling, C.; Schaffer, J.; Seidel, C. a. M.; Korte, J.; Brehm, G.; Schneider, S.; Schrof, W. Homogeneity, Transport, and Signal Properties of Single Ag Particles Studied by Single-Molecule Surface-

DOI: 10.1021/acsnano.6b03796
ACS Nano 2016, 10, 8552−8563

Enhanced Resonance Raman Scattering. *J. Phys. Chem. A* **2001**, *105*, 3673−3679.
(6) Stockman, M. I. Nanoscience: Dark-Hot Resonances. *Nature* **2010**, *467*, 541−542.
(7) Barrow, S. J.; Wei, X.; Baldauf, J. S.; Funston, A. M.; Mulvaney, P. The Surface Plasmon Modes of Self-Assembled Gold Nanocrystals. *Nat. Commun.* **2012**, *3*, 1275.
(8) Shalaev, V. M. Optical Negative-Index Metamaterials. *Nat. Photonics* **2007**, *1*, 41−48.
(9) Alu, A.; Engheta, N. The Quest for Magnetic Plasmons at Optical Frequencies. *Opt. Express* **2009**, *17*, 5723−5730.
(10) Prodan, E.; Radloff, C.; Halas, N. J.; Nordlander, P. A Hybridization Model for the Plasmon Response of Complex Nanostructures. *Science* **2003**, *302*, 419−422.
(11) Chuntonov, L.; Haran, G. Trimeric Plasmonic Molecules: The Role of Symmetry. *Nano Lett.* **2011**, *11*, 2440−2445.
(12) Chuntonov, L.; Haran, G. Effect of Symmetry Breaking on the Mode Structure of Trimeric Plasmonic Molecules. *J. Phys. Chem. C* **2011**, *115*, 19488−19495.
(13) Lee, H.; Kim, G.-H.; Lee, J.-H.; Kim, N. H.; Nam, J.-M.; Suh, Y. D. Quantitative Plasmon Mode and Surface-Enhanced Raman Scattering Analyses of Strongly Coupled Plasmonic Nanotrimers with Diverse Geometries. *Nano Lett.* **2015**, *15*, 4628−4636.
(14) Kumar, J.; Wei, X.; Barrow, S.; Funston, A. M.; Thomas, K. G.; Mulvaney, P. Surface Plasmon Coupling in End-to-End Linked Gold Nanorod Dimers and Trimers. *Phys. Chem. Chem. Phys.* **2013**, *15*, 4258−4264.
(15) Funston, A.; Davis, T. J.; Novo, C.; Mulvaney, P. Coupling Modes of Gold Trimer Superstructures. *Philos. Trans. R. Soc., A* **2011**, *369*, 3472−3482.
(16) Funston, A. M.; Novo, C.; Davis, T. J.; Mulvaney, P. Plasmon Coupling of Gold Nanorods at Short Distances and in Different Geometries. *Nano Lett.* **2009**, *9*, 1651−8.
(17) Barrow, S. J.; Rossouw, D.; Funston, A. M.; Botton, G. A.; Mulvaney, P. Mapping Bright and Dark Modes in Gold Nanoparticle Chains using Electron Energy Loss Spectroscopy. *Nano Lett.* **2014**, *14*, 3799−3808.
(18) Koh, A. L.; Bao, K.; Khan, I.; Smith, W. E.; Kothleitner, G.; Nordlander, P.; Maier, S. A.; McComb, D. W. Electron Energy-Loss Spectroscopy (EELS) of Surface Plasmons in Single Silver Nanoparticles and Dimers: Influence of Beam Damage and Mapping of Dark Modes. *ACS Nano* **2009**, *3*, 3015−3022.
(19) Fujimoto, F.; Komaki, K.-i.; Ishida, K. Surface Plasma Oscillation in Aluminum Fine Particles. *J. Phys. Soc. Jpn.* **1967**, *23*, 1186.
(20) Fujimoto, F.; Komaki, K.-i. Plasma Oscillations Excited by a Fast Electron in a Metallic Particle. *J. Phys. Soc. Jpn.* **1968**, *25*, 1679−1687.
(21) Kreibig, U.; Zacharias, P. Surface Plasma Resonances in Small Spherical Silver and Gold Particles. *Eur. Phys. J. A* **1970**, *231*, 128−143.
(22) Bosman, M.; Keast, V. J.; Watanabe, M.; Maaroof, A. I.; Cortie, M. B. Mapping Surface Plasmons at the Nanometre Scale with an Electron Beam. *Nanotechnology* **2007**, *18*, 165505.
(23) Nelayah, J.; Kociak, M.; Stephan, O.; Garcia de Abajo, F. J.; Tence, M.; Henrard, L.; Taverna, D.; Pastoriza-Santos, I.; Liz-Marzan, L. M.; Colliex, C. Mapping Surface Plasmons on a Single Metallic Nanoparticle. *Nat. Phys.* **2007**, *3*, 348−353.
(24) Novo, C.; Funston, A. M.; Pastoriza-Santos, I.; Liz-Marzan, L. M.; Mulvaney, P. Spectroscopy and High-Resolution Microscopy of Single Nanocrystals by a Focused Ion Beam Registration Method. *Angew. Chem., Int. Ed.* **2007**, *46*, 3517−3520.
(25) Henry, A.-I.; Bingham, J. M.; Ringe, E.; Marks, L. D.; Schatz, G. C.; Van Duyne, R. P. Correlated Structure and Optical Property Studies of Plasmonic Nanoparticles. *J. Phys. Chem. C* **2011**, *115*, 9291−9305.
(26) Nehl, C. L.; Grady, N. K.; Goodrich, G. P.; Tam, F.; Halas, N. J.; Hafner, J. H. Scattering Spectra of Single Gold Nanoshells. *Nano Lett.* **2004**, *4*, 2355−2359.
(27) Billaud, P.; Marhaba, S.; Cottancin, E.; Arnaud, L.; Bachelier, G.; Bonnet, C.; Del Fatti, N.; Valle, F.; Vialle, J.; Broyer, M.; Pellarin, M. Correlation Between the Extinction Spectrum of a Single Metal Nanoparticle and Its Electron Microscopy Image. *J. Phys. Chem. C* **2008**, *112*, 978−982.
(28) Ringe, E.; Langille, M. R.; Sohn, K.; Zhang, J.; Huang, J.; Mirkin, C. A.; Van Duyne, R. P.; Marks, L. D. Plasmon Length: A Universal Parameter to Describe Size Effects in Gold Nanoparticles. *J. Phys. Chem. Lett.* **2012**, *3*, 1479−1483.
(29) Scholl, J. a.; Koh, A. L.; Dionne, J. a. Quantum Plasmon Resonances of Individual Metallic Nanoparticles. *Nature* **2012**, *483*, 421−7.
(30) Yamamoto, N.; Ohtani, S.; García de Abajo, F. J. Gap and Mie Plasmons in Individual Silver Nanospheres Near a Silver Surface. *Nano Lett.* **2011**, *11*, 91−5.
(31) Chu, M.-W.; Myroshnychenko, V.; Chen, C. H.; Deng, J.-P.; Mou, C.-Y.; Garcia de Abajo, F. J. Probing Bright and Dark Surface-Plasmon Modes in Individual and Coupled Noble Metal Nanoparticles Using an Electron Beam. *Nano Lett.* **2009**, *9*, 399−404.
(32) Nicoletti, O.; de la Pena, F.; Leary, R. K.; Holland, D. J.; Ducati, C.; Midgley, P. A. Three-Dimensional Imaging of Localized Surface Plasmon Resonances of Metal Nanoparticles. *Nature* **2013**, *502*, 80−84.
(33) Collins, S. M.; Ringe, E.; Duchamp, M.; Saghi, Z.; Dunin-Borkowski, R. E.; Midgley, P. A. Eigenmode Tomography of Surface Charge Oscillations of Plasmonic Nanoparticles by Electron Energy Loss Spectroscopy. *ACS Photonics* **2015**, *2*, 1628−1635.
(34) Rossouw, D.; Couillard, M.; Vickery, J.; Kumacheva, E.; Botton, G. A. Multipolar Plasmonic Resonances in Silver Nanowire Antennas Imaged with a Subnanometer Electron Probe. *Nano Lett.* **2011**, *11*, 1499−1504.
(35) Rossouw, D.; Botton, G. a. Resonant Optical Excitations in Complementary Plasmonic Nanostructures. *Opt. Express* **2012**, *20*, 6968−73.
(36) Rossouw, D.; Botton, G. Plasmonic Response of Bent Silver Nanowires for Nanophotonic Subwavelength Waveguiding. *Phys. Rev. Lett.* **2013**, *110*, 066801.
(37) Collins, S. M.; Nicoletti, O.; Rossouw, D.; Ostasevicius, T.; Midgley, P. A. Excitation Dependent Fano-Like Interference Effects in Plasmonic Silver Nanorods. *Phys. Rev. B: Condens. Matter Mater. Phys.* **2014**, *90*, 155419.
(38) N'Gom, M.; Li, S.; Schatz, G.; Erni, R.; Agarwal, A.; Kotov, N.; Norris, T. B. Electron-Beam Mapping of Plasmon Resonances in Electromagnetically Interacting Gold Nanorods. *Phys. Rev. B: Condens. Matter Mater. Phys.* **2009**, *80*, 113411.
(39) Scholl, J. A.; Garcia-Etxarri, A.; Aguirregabiria, G.; Esteban, R.; Narayan, T. C.; Koh, A. L.; Aizpurua, J.; Dionne, J. A. Evolution of Plasmonic Metamolecule Modes in the Quantum Tunneling Regime. *ACS Nano* **2016**, *10*, 1346−1354.
(40) Lin, C.-J. Projected Gradient Methods for Nonnegative Matrix Factorization. *Neural Comput.* **2007**, *19*, 2756−2779.
(41) Lee, D. D.; Seung, H. S. Learning the Parts of Objects by Non-Negative Matrix Factorization. *Nature* **1999**, *401*, 788−791.
(42) Johnson, P. B.; Christy, R. W. Optical Constants of the Noble Metals. *Phys. Rev. B* **1972**, *6*, 4370−4379.
(43) Collins, S. M.; Midgley, P. A. Surface Plasmon Excitations in Metal Spheres: Direct Comparison of Light Scattering and Electron Energy-Loss Spectroscopy by Modal Decomposition. *Phys. Rev. B: Condens. Matter Mater. Phys.* **2013**, *87*, 235432.
(44) Mazzucco, S.; Geuquet, N.; Ye, J.; Stéphan, O.; Van Roy, W.; Van Dorpe, P.; Henrard, L.; Kociak, M. Ultralocal Modification of Surface Plasmons Properties in Silver Nanocubes. *Nano Lett.* **2012**, *12*, 1288−1294.
(45) de la Peña, F.; Berger, M.-H.; Hochepied, J.-F.; Dynys, F.; Stephan, O.; Walls, M. Mapping Titanium and Tin Oxide Phases using EELS: An Application of Independent Component Analysis. *Ultramicroscopy* **2011**, *111*, 169−176.
(46) Sheikholeslami, S. N.; Garcia-Etxarri, A.; Dionne, J. A. Controlling the Interplay of Electric and Magnetic Modes via Fano-Like Plasmon Resonances. *Nano Lett.* **2011**, *11*, 3927−3934.

DOI: 10.1021/acsnano.6b03796
ACS Nano 2016, 10, 8552−8563

(47) Boudarham, G.; Kociak, M. Modal Decompositions of the Local Electromagnetic Density of States and Spatially Resolved Electron Energy Loss Probability in Terms of Geometric Modes. *Phys. Rev. B: Condens. Matter Mater. Phys.* **2012**, *85*, 245447.
(48) Rodríguez-Fernández, J.; Pérez-Juste, J.; Garcia de Abajo, F. J.; Liz-Marzán, L. M. Seeded Growth of Submicron Au Colloids with Quadrupole Plasmon Resonance Modes. *Langmuir* **2006**, *22*, 7007−7010.
(49) Yao, H.; Yi, C.; Tzang, C.-H.; Zhu, J.; Yang, M. DNA-Directed Self-Assembly of Gold Nanoparticles into Binary and Ternary Nanostructures. *Nanotechnology* **2007**, *18*, 015102.
(50) Maigne, A.; Twesten, R. D. Review of Recent Advances in Spectrum Imaging and its Extension to Reciprocal Space. *J. Electron Microsc.* **2009**, *58*, 99−109.
(51) Hohenester, U.; Trugler, A. MNPBEM, A Matlab Toolbox for the Simulation of Plasmonic Nanoparticles. *Comput. Phys. Commun.* **2012**, *183*, 370−381.

DOI: 10.1021/acsnano.6b03796
ACS Nano 2016, 10, 8552−8563